Vector Magnetometer Based on a Single Spin-Orbit-Torque Anomalous-Hall Device

Xin Chen,[1] Hang Xie,[1] Haoxuan Shen,[1,2] and Yihong Wu[1,*]

[1] *Department of Electrical and Computer Engineering, National University of Singapore, Singapore 117583, Singapore*

[2] *National University of Singapore (Chong Qing) Research Institute, Chongqing Liang Jiang New Area, Chongqing 401123, China*

(Received 21 April 2022; revised 20 June 2022; accepted 11 July 2022; published 3 August 2022)

In many applications, the ability to measure the vector information of a magnetic field with high spatial resolution and low cost is essential, but remains a challenge for existing magnetometers composed of multiple sensors. Here, we report a single-device based vector magnetometer, which is enabled by spin-orbit torque, capable of measuring a vector magnetic field using the harmonic Hall resistances of a ferromagnet (FM)/heavy metal (HM) bilayer with superparamagnetic behavior. Under an ac driving current, the first- and second-harmonic Hall resistances of the FM/HM bilayer show a linear relationship with the vertical and longitudinal component (along the current direction) of the magnetic field, respectively. By employing an L-shaped Hall device with two orthogonal arms, we can measure all the three field components simultaneously, thereby detecting both the amplitude and direction of magnetic field in a three-dimensional space. As proofs of concepts, we demonstrate both angular position sensing on the three coordinate planes and vector mapping of magnetic field generated by a permanent magnet, both of which are in good agreement with the simulation results. Crosstalk between vertical and longitudinal field components at large field is discussed using theoretical models.

DOI: 10.1103/PhysRevApplied.18.024010

I. INTRODUCTION

Advancements in magnetic sensing have contributed immensely to a wide range of scientific and technological fields from fundamental physics, chemistry, and biology to practical applications such as data storage and medical imaging, but measurement of a vector field with high spatial resolution using a single magnetic sensor remains challenging. Compact and low-cost magnetometers such as Hall and magnetoresistance (MR) sensors are readily available [1–7], but these sensors only detect the magnetic field in a specific direction. To detect the field components in three orthogonal directions in space simultaneously, a common method is to integrate three magnetic sensors whose detection axes are perpendicular to each other [8–14] or to use a magnetic flux guide to change the direction of one of the field components [12,15,16], as shown schematically in Figs. 1(a) and 1(b). However, these techniques often suffer from either, or a combination of, high cost, large size, low spatial resolution, high noise, and crosstalk among the measurement axes. The recently reported nitrogen-vacancy magnetometer does provide good spatial resolution, but it requires sophisticated optics and an expensive microwave source to operate, making it unsuitable for cost-sensitive applications [17–19].

In this work, we propose and experimentally demonstrate a high-spatial-resolution and low-cost vector magnetometer, which we call a harmonic Hall vector magnetometer, based on a single Hall device enabled by spin-orbit torque (SOT) [20–24]. The sensor has an extremely simple structure, which consists of just an L-shaped $Co_{20}Fe_{60}B_{20}$/Ta Hall bar with two mutually perpendicular arms (to facilitate discussion, hereafter we refer them to as arm-X and arm-Y), as shown in Fig. 1(c). The thickness of $Co_{20}Fe_{60}B_{20}$ is optimized such that it exhibits small perpendicular magnetic anisotropy (PMA) with superparamagnetic behavior near room temperature [25–29], as confirmed by anomalous Hall effect (AHE) and magnetometry measurements. We apply an ac current to the Hall device and measure the first- and second-harmonic components of the AHE signal from both arms. At small field, the former is proportional to the out-of-plane (OP) component (H_z) of the external field whereas the latter is proportional to the in-plane (IP) component (H_x or H_y) along the driving current direction due to a damping-like (DL) SOT effective field. As current directions are perpendicular to each other in the two arms of the L-shaped Hall device, one can simultaneously determine H_x and H_y from the second-harmonic AHE signal of the respective arms and

*elewuyh@nus.edu.sg

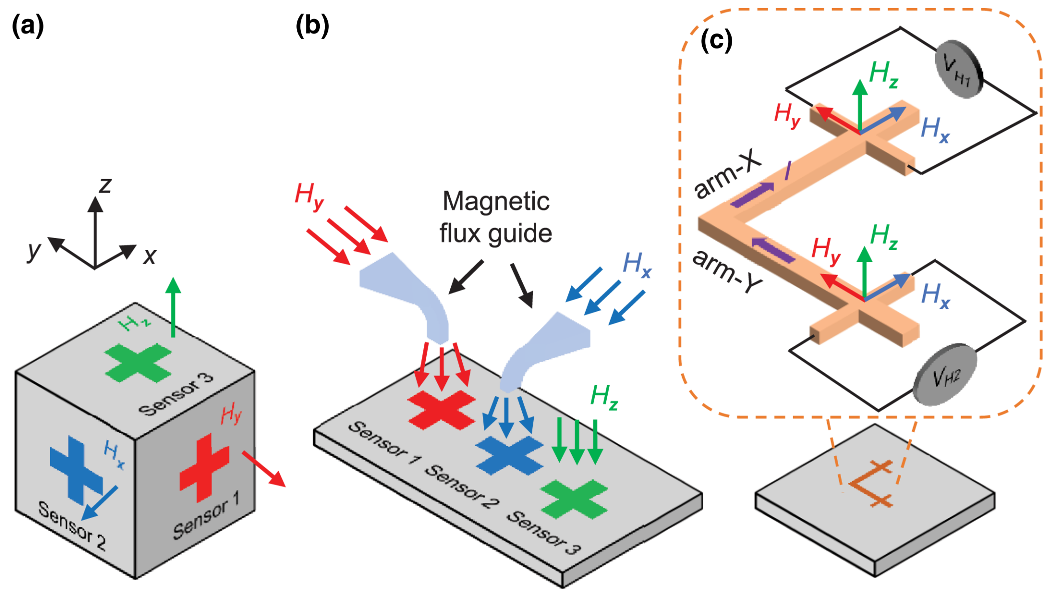

FIG. 1. Schematics of: (a) vector magnetometer using multiple sensors; (b) vector magnetometer with multiple sensors and magnetic flux guide; (c) vector magnetometer presented in this work. Purple arrows indicate the current directions.

H_z from the first-harmonic AHE signal of either arm. In this way, we realize precise measurement of the three field components simultaneously using a single device without any post-measurement data processing. The linearity ranges for the IP and OP components are ± 100 Oe and ± 50 Oe, respectively, which make the sensor suitable for a wide range of applications. As proof-of-concept applications, we demonstrate both angular position detection and vector field mapping using the developed sensor. The average angle error across 360° is less than 1° in the three Cartesian coordinate planes, and the vector mapping of the magnetic field generated by a cylindrical magnet agrees well with the simulation results. Crosstalk between vertical and longitudinal field components at large field is discussed using theoretical models.

II. OPERATION PRINCIPLE AND EXPERIMENTAL DETAILS

A. Principle of a harmonic Hall vector magnetometer

In general, the hysteresis (or M–H) loop of ferromagnetic materials may be modeled using the hyperbolic analytical approximation of the Everett integral based on the stochastic Preisach approach [30,31]. According to this model, the ascending M_a and descending M_d branches of the M–H loop may be expressed as

$$M_a = M_s \tanh\left[\frac{1}{H_0}(H - H_c)\right] + F(H_m), \tag{1}$$

$$M_d = M_s \tanh\left[\frac{1}{H_0}(H + H_c)\right] - F(H_m), \tag{2}$$

where M_s is the saturation magnetization, H_c is coercivity, H_m is the maximum excitation field, $1/H_0$ is the differential permeability at $H = H_c$, and $F(H_m) = (M_S/2)\{\tanh[(H_m + H_c)/H_0] - \tanh[(H_m - H_c)/H_0]\}$. When the coercivity is negligible and the loop is symmetrical at large fields, i.e., $H_c = 0$ and $F(H_m) = 0$, M_a and M_d can be written as

$$M_a = M_d = M_s \tanh\frac{H}{H_0}. \tag{3}$$

Thin films with such kind of magnetic properties have been employed to realize superparamagnetic tunnel junctions [32–36]. In the present case, the L-shaped device consists of a $Co_{20}Fe_{60}B_{20}$/Ta bilayer with weak PMA and negligible hysteresis, and we use it to detect the vector information of magnetic field. When the bilayer is subjected to both an external magnetic field along the z-axis (i.e., easy axis) and an IP current along the x-axis, the vertical component of the magnetization can be written as $M_z = M_S\tanh(H_z^{\text{eff}}/H_0)$, where H_z^{eff} is the effective magnetic field along the z-axis, including both external field (H_z) and the DL SOT effective field, i.e., $H_z^{\text{eff}} = H_z + H_z^{\text{DL}}$. The H_z^{DL} is known to be proportional to the projection of magnetization along current direction, i.e., $H_z^{\text{DL}} = H^{\text{DL}} m_x$ with H^{DL} the magnitude of DL effective field and m_x the normalized magnetization in the x-direction [20]. The H_z^{DL} functions as an effective "knob" to detect longitudinal field H_x as when H_x is small, $H_z^{\text{DL}} \approx (H^{\text{DL}}/H_k^{\text{eff}})H_x$, where H_k^{eff} is the effective anisotropy field [37–42]. As the $Co_{20}Fe_{60}B_{20}$/Ta bilayer exhibits PMA, the anomalous resistance R_H can be written as

$$R_H = R_0 + R_{\mathrm{AHE}}\tanh\left[\frac{1}{H_0}\left(H_z + \frac{H^{\mathrm{DL}}}{H_k^{\mathrm{eff}}}H_x\right)\right], \quad (4)$$

where R_{AHE} is AHE resistance at saturation and R_0 is the offset resistance induced by misalignment of Hall voltage electrodes.

When the sensor is driven by an ac current $I = I_0 \sin \omega t$, the DL effective field can be written as $H_{\mathrm{DL}} = (\hbar/2e)[\theta_{\mathrm{SH}}/(M_S t_{\mathrm{FM}} S)] I_0 \sin \omega t$, where θ_{SH} is the effective spin Hall angle of Ta, t_{FM} is the thickness of $Co_{20}Fe_{60}B_{20}$ layer, S is the cross-section area of the device, I_0 and ω are the amplitude and angular frequency of the ac current, respectively, $\hbar$ is the reduced Planck constant, and e is the electron charge [42]. From Eq. (4), we can obtain the Hall voltage for the Hall cross of arm-X as

$$\begin{aligned} V_H &= I_0 \sin \omega t R_0 + I_0 \sin \omega t R_{\mathrm{AHE}}\tanh\left[\frac{1}{H_0}\left(H_z + \frac{\hbar}{2e}\frac{\theta_{\mathrm{SH}}}{M_S t_{\mathrm{FM}} S}\frac{H_x}{H_k^{\mathrm{eff}}} I_0 \sin \omega t\right)\right] \\ &= I_0 \sin \omega t R_0 + I_0 \sin \omega t R_{\mathrm{AHE}}\tanh\left[\frac{1}{H_0}(H_z + A H_x I_0 \sin \omega t)\right] \\ &= I_0 R_0 \sin \omega t + I_0 R_{\mathrm{AHE}} \sin \omega t \sum_{n=1}^{\infty} \frac{2^{2n}(2^{2n}-1)B_{2n}[(1/H_0)(H_z + A H_x I_0 \sin \omega t)]^{2n-1}}{(2n)!}, \end{aligned} \quad (5)$$

where $A = (\hbar/2e)[\theta_{\mathrm{SH}}/(M_s t_{\mathrm{FM}} S H_k^{\mathrm{eff}})]$ and B_n is nth Bernoulli number. When both H_z and H_x are small, terms with $n \geq 2$ in Eq. (5) are negligible and Eq. (5) can be reduced to

$$\begin{aligned} V_H &\approx \left(I_0 R_0 + \frac{I_0 R_{\mathrm{AHE}}}{H_0} H_z\right) \sin \omega t + \left(I_0^2 \frac{R_{\mathrm{AHE}}}{H_0} A H_x\right)(\sin \omega t)^2 \\ &= \frac{1}{2} I_0^2 \frac{R_{\mathrm{AHE}}}{H_0} A H_x + I_0\left(R_0 + \frac{R_{\mathrm{AHE}}}{H_0} H_z\right) \sin \omega t - \frac{1}{2} I_0^2 \frac{R_{\mathrm{AHE}}}{H_0} A H_x \cos 2\omega t. \end{aligned} \quad (6)$$

As can be seen from Eq. (6), the amplitudes of the first and second harmonic V_H are linearly proportional to H_z and H_x, respectively, which facilitates the discrimination of H_z and H_x contributions to the output signal. The same results also apply to arm-Y by simply replacing H_x with H_y. By doing so, we can detect H_x, H_y, and H_z simultaneously using a single device. In deriving the above equations, we have ignored the planar Hall effect because we found that it was negligible experimentally.

B. Sample preparation and experimental methods

Stack of $MgO(1.1)/Co_{20}Fe_{60}B_{20}(t_{\mathrm{CoFeB}})/Ta(1.1)/MgO(2)/Ta(1.5)$ (the numbers in parentheses indicate the layer thickness in nanometers) thin films were deposited on the Si/SiO_2 substrates by magnetron sputtering with a base pressure of 1×10^{-8} Torr and a working pressure of 3×10^{-3} Torr. Here, t_{CoFeB} is the thickness of the $Co_{20}Fe_{60}B_{20}$ layer. The Microtech LaserWriter system with a 405 nm laser was used to directly expose the photoresist (Microposit S1805), after which it was developed in MF319 to form the L-shaped Hall bar pattern. After film deposition, the photoresist was removed by a mixture of Remover PG and acetone to complete the Hall device fabrications. The processes of photography and lift-off were repeated to form electrodes and contact pads with the layers of $Ta(5)/Cu(150)/Pt(10)$ for Hall bars. Finally, the devices were all annealed at 250 °C for 1 h in a vacuum furnace with a pressure $< 1 \times 10^{-5}$ Torr to improve PMA [43–46]. The electrical measurements were performed in the Quantum Design VersaLab PPMS with a sample rotator. The ac or dc current was applied by Keithley 6221 current source. The Hall voltage was measured by the Keithley 2182 nanovoltmeter (for dc voltage) and the 500 kHz MFLI lock-in amplifier from Zurich Instruments (for harmonic voltages). Vector mapping of magnetic field generated by a permanent magnet was performed using an xy stage in a normal experimental room.

III. RESULTS AND DISCUSSION

A. Thickness optimization and current-induced switching of $MgO/Co_{20}Fe_{60}B_{20}/Ta$

Prior to the device fabrication, the thickness of $Co_{20}Fe_{60}B_{20}$ film has been optimized to reduce the coercivity to nearly zero [47–53]. Figure 2(a) shows the

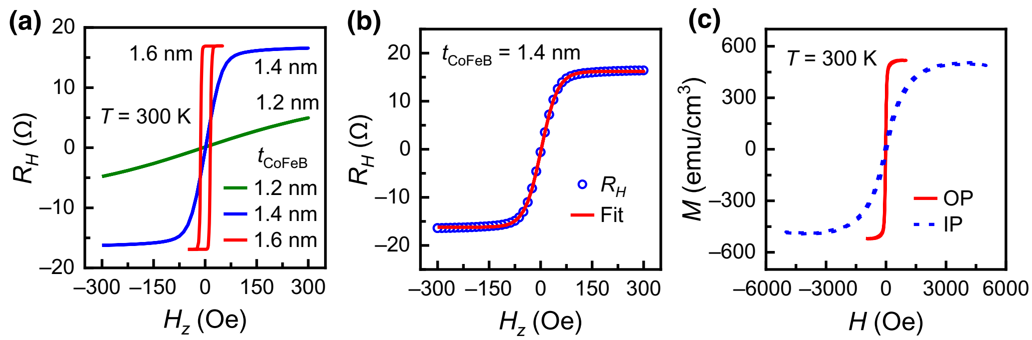

FIG. 2. (a) AHE loops for MgO(1.1)/$Co_{20}Fe_{60}B_{20}$(t_{CoFeB})/Ta(1.1)/MgO(2)/Ta(1.5) multilayers with $t_{\mathrm{CoFeB}} = 1.2$ (green), 1.4 (blue), and 1.6 (red). (b) AHE loop of MgO(1.1)/$Co_{20}Fe_{60}B_{20}$(1.4)/Ta(1.1)/MgO(2)/Ta(1.5) at a dc current 1 mA and at room temperature. Measured data (circle) is fitted with Eq. (4) (solid line). (c) M–H curves for MgO(1.1)/$Co_{20}Fe_{60}B_{20}$(1.4)/Ta(1.1)/MgO(2)/Ta(1.5) multilayers with OP (red solid line) and IP (blue dashed line) magnetic field at 300 K.

AHE loops for MgO(1.1)/$Co_{20}Fe_{60}B_{20}$(t_{CoFeB})/Ta(1.1)/MgO(2)/Ta(1.5) multilayers with different $Co_{20}Fe_{60}B_{20}$ thicknesses (t_{CoFeB}= 1.2, 1.4, and 1.6) at room temperature. As can be seen, the sample with 1.4 nm $Co_{20}Fe_{60}B_{20}$ exhibits an AHE loop with sizable AHE resistance and negligible hysteresis, whereas the sample with 1.2 nm $Co_{20}Fe_{60}B_{20}$ exhibits a significantly decreased AHE and the sample with 1.6 nm $Co_{20}Fe_{60}B_{20}$ exhibits an AHE loop with a hysteresis, which is undesired for a linear field sensor. Therefore, 1.4 nm $Co_{20}Fe_{60}B_{20}$ exhibited the superparamagnetic behavior at room temperature and it is used as an FM layer in the developed sensor. In typical AHE measurements with small current, H^{DL} can be ignored and Eq. (4) can be written as $R_H = R_0 + R_{\mathrm{AHE}}\tanh[H_z/H_0]$, which fits well the measured AHE curve in MgO(1.1)/$Co_{20}Fe_{60}B_{20}$(1.4)/Ta(1.1)/MgO(2)/Ta(1.5) with the parameters $R_{\mathrm{AHE}} = 16.24\ \Omega$, $R_0 = 0.09\ \Omega$, and $H_0 = 49.60$ Oe, as shown in Fig. 2(b). The results confirm the validity of Eq. (4) for describing the AHE of the bilayer structure used in this study. As can be seen from the M–H loops in Fig. 2(c), the thin film exhibits weak PMA with negligible hysteresis.

After thickness optimization, we proceeded to fabricate the L-shaped device as shown schematically in Fig. 1(c). The width and length of each arm are 15 and 120 μm, respectively. Figure 3(a) shows the anomalous Hall resistance (R_H) in arm-X and arm-Y as a function of external field H_z measured at an applied dc current of 1 mA for MgO(1.1)/$Co_{20}Fe_{60}B_{20}$(1.4)/Ta(1.1)/MgO(2)/Ta(1.5). As can be seen, both arms of the device exhibit AHE with the coercivity of 0 Oe and R_{AHE} of 16.2 Ω at room temperature, indicating good film uniformity in the whole device. The β-Ta buffer layer with a resistivity of 170.6 $\mu\Omega$ cm is used to generate spin current due to spin Hall effect. Furthermore, Fig. 3(b) shows the current-induced switching loops of arm-X with different H_x at room temperature. As can be seen, the switching loops corroborate well with the SOT mechanism. When $H_x = 0$, no current-induced switching occurs. The switching ratio increases with increasing H_x, and the switching polarity is determined by the directions of both I_x and H_x. The switching saturates at 3.85 mA. The current-induced Hall resistance difference ΔR_H between ±3.85 mA at different H_x is summarized in Fig. 3(c) (circle), which can be well fitted with $\Delta R_H = \Delta R_0\ \tanh\{I_0(1/H_0)(\hbar/2e)[\theta_{\mathrm{SH}}/(M_s t_{\mathrm{FM}} S H_k^{\mathrm{eff}})]H_x\}$ (solid line), where $\Delta R_0 = 4.92\ \Omega$, $\theta_{\mathrm{SH}} = -0.07$, $I_0 = 4.05$ mA, $M_s = 500.1$ emu/cm^3, and $H_k^{\mathrm{eff}} = 699.91$ Oe. This agrees well with Eq. (4) with $H_z = 0$. Figure 3(d) shows the second-harmonic Hall resistance as a function H_x with different driving current. As can be seen, the output signal increases with driving current amplitude and saturates around 4 mA, which agrees well with the current value required for saturating the switching ratio in Fig. 3(b).

B. Measurements of individual field component

To demonstrate the proof-of-concept operation of the harmonic Hall vector magnetometer, we first conducted the harmonic Hall measurements on the L-shaped device when the external magnetic field was swept along three orthogonal axes separately. Harmonic Hall resistance is defined by the harmonic Hall voltage divided by the applied current amplitude. Figure 4 shows the first- and second-harmonic Hall resistance as a function of sweeping fields in x-, y-, and z-direction, respectively. The device was driven by an ac current with an amplitude of 4 mA and frequency of 115 Hz to obtain maximum output. The first- and second-harmonic Hall voltages were acquired using the lock-in amplifier. In Fig. 4(a) the harmonic Hall resistances, R_{H1}^{ω} and $R_{H1}^{2\omega}$, of arm-X are shown when the field is swept along the z-direction (note: zero-field offset has been subtracted out). As can be seen, R_{H1}^{ω} is linear to the H_z at small field and saturates at high field, whereas the amplitude of $R_{H1}^{2\omega}$ is almost zero in the entire field range. Figure 4(d) displays $R_{H1}^{\omega} - H_z$ in a smaller range from −50 Oe to

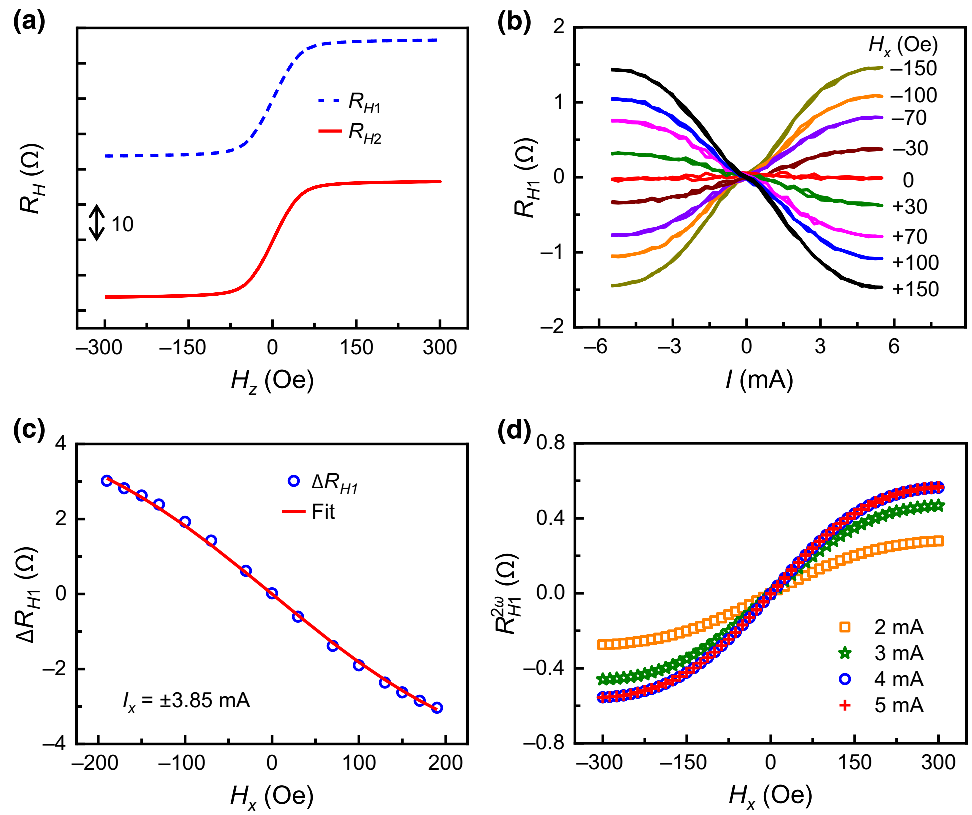

FIG. 3. (a) AHE loops of arm-X (upper curve) and arm-Y (lower curve) measured at a dc current of 1 mA at room temperature. (b) Current-induced switching loops of arm-X measured at different assistive fields, H_x. (c) Current-induced Hall resistance difference at ±3.85 mA with different H_x (circle, experiment; solid line, fitting). (d) Second-harmonic Hall resistance obtained at different current amplitude: 2 mA (orange square), 3 mA (green star), 4 mA (blue circle), and 5 mA (red cross).

+50 Oe. Within this range, the curve shows good linearity with the maximum linearity error less than 3%, negligible hysteresis and a sensitivity of 149.44 mΩ/Oe. An opposite trend is obtained when the field sweeps in the x-direction, as shown in Fig. 4(b). In this case, $R^{2\omega}_{H1}$ is linear with respect to H_x at small field and saturates at high field. Although a small R^{ω}_{H1} is also observed, it could be due to misalignment of field in this measurement. As can be seen from Fig. 4(e), $R^{2\omega}_{H1}$ exhibits good linearity with maximum linearity error less than 3%, negligible hysteresis, and a sensitivity of 3.36 mΩ/Oe in the field range of −100 Oe to +100 Oe. The much smaller sensitivity compared with R^{ω}_{H1} obtained by sweeping the field in z-direction is expected as it is a second-order effect. Similar results were obtained for arm-Y, as shown in Figs. 4(c) and 4(f). In this case, the field was swept in y-direction. As expected, $R^{2\omega}_{H2}$ is linear to H_y at small field and saturates at large field, whereas R^{ω}_{H2} is nearly zero in the entire field range. The sensitivity, 3.30 mΩ/Oe, and linear range, −100 Oe to +100 Oe, are similar to those of arm-X, indicating good uniformity in both the film stack and patterned device. The results indicate that the L-shaped device functions well as a linear sensor when there is only one field component present.

C. Angle detection on three coordinate planes

Next, we examine the possibility of using the L-shaped device as a biaxial sensor. Owing to the unavailability of a vector electromagnet, here we use the Hall device to determine the direction of a magnetic field with constant magnitude but with its direction rotating in the three coordinate planes. As shown schematically in Figs. 5(a)–5(c), when the field rotates in the zx, yz, and xy planes, the first- and second-harmonic Hall resistance are given by (i) rotation in the zx plane, $R^{\omega}_{H1} = R_0 + R_{\mathrm{AHE}}H\cos\theta^H_{zx}/H_0$, $R^{2\omega}_{H1} = -(I_0R_{\mathrm{AHE}}AH\sin\theta^H_{zx})/(2H_0)$; (ii) rotation in the yz plane, $R^{\omega}_{H2} = R_0 + R_{\mathrm{AHE}}H\sin\theta^H_{yz}/H_0$, $R^{2\omega}_{H2} = -(I_0R_{\mathrm{AHE}}AH\cos\theta^H_{yz})/(2H_0)$; and (iii) rotation in the xy plane, $R^{2\omega}_{H1} = -(I_0R_{\mathrm{AHE}}AH\cos\theta^H_{xy})/(2H_0)$, $R^{2\omega}_{H2} = -(I_0R_{\mathrm{AHE}}AH\sin\theta^H_{xy})/(2H_0)$. Here, H is the external magnetic field amplitude, θ^H_{zx}, θ^H_{yz}, and θ^H_{xy} are the angles between the rotating field and the z-, y-, and x-axis, respectively, on the zx, yz, and xy plane. The angle is positive when the rotation direction and axis follows the right-handed rule.

Figure 5(d) shows R^{ω}_{H1} and $R^{2\omega}_{H1}$ as a function of θ^H_{zx} from 0° to 360° when the device is driven by an ac current with an amplitude of 4 mA and frequency of 115 Hz. The external field strength is 10 Oe. Both

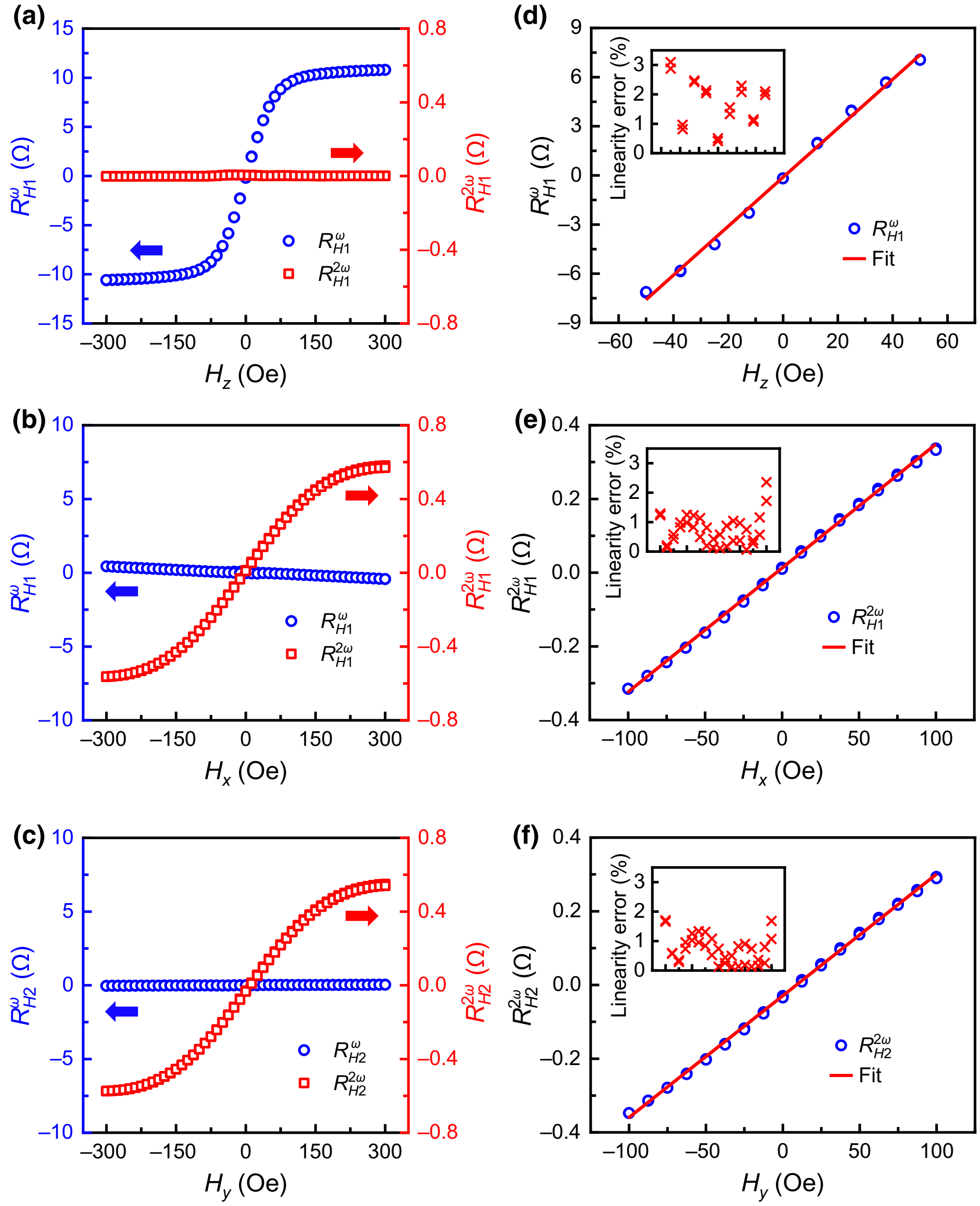

FIG. 4. (a)–(c) First-harmonic (circle) and second-harmonic (square) Hall resistance with the field swept in (a) z-direction (arm-X), (b) x-direction (arm-X), and (c) y-direction (arm-Y), respectively. (d)–(f) Harmonic Hall resistance as a function of external field H_x, H_y, and H_z, respectively, in the small field range. Solid lines are linear fittings with the linearity error given in the insets.

signals were acquired from the single device simultaneously using the lock-in amplifier. As expected, the $R^{\omega}_{H1} - \theta^{H}_{zx}$ curve is in a cosine shape whereas $R^{2\omega}_{H1} - \theta^{H}_{zx}$ follows a sine function. They can be fitted well with $R^{\omega}_{H10} \cos \theta^{H}_{zx}$ (solid line in blue) and $R^{2\omega}_{H10} \sin \theta^{H}_{zx}$ (solid line in red), respectively, where R^{ω}_{H10} and $R^{2\omega}_{H10}$ are the amplitudes of $R^{\omega}_{H1} - \theta^{H}_{zx}$ and $R^{2\omega}_{H1} - \theta^{H}_{zx}$ curves, respectively. Similar results are obtained for the field rotating in the yz and xy planes, as shown in Figs. 5(e) and 5(f), respectively. The field strength remains as 10 Oe. With the sine and cosine dependence of the harmonic Hall resistance, we can calculate the field angle as $\theta_{zx} = \text{atan2}(-R^{\omega}_{H1}/R^{\omega}_{H10}, -R^{2\omega}_{H1}/R^{2\omega}_{H10}) + \pi$, $\theta_{yz} = \text{atan2}(-R^{2\omega}_{H2}/R^{2\omega}_{H20}, -R^{\omega}_{H2}/R^{\omega}_{H20}) + \pi$, and $\theta_{xy} = \text{atan2}(-R^{2\omega}_{H1}/R^{2\omega}_{H10}, -R^{2\omega}_{H2}/R^{2\omega}_{H20}) + \pi$. Figures 5(g)–5(i) show the relationship between the detected angle and actual field angle on the three coordinate planes. As can be seen, the detected angle is almost the same as the actual angle. As shown in the insets, the maximum angle error is around 3°, and the average error from 0 to 360° is less than 1°.

Next, we turn to the field angle detections at large magnetic fields. Figure 6(a) shows R^{ω}_{H1} and $R^{2\omega}_{H1}$ as a function of θ^{H}_{zx} from 0° to 360° when the external field strength is 30 Oe, whereas Fig. 6(b) shows $R^{2\omega}_{H1}$ and $R^{2\omega}_{H2}$

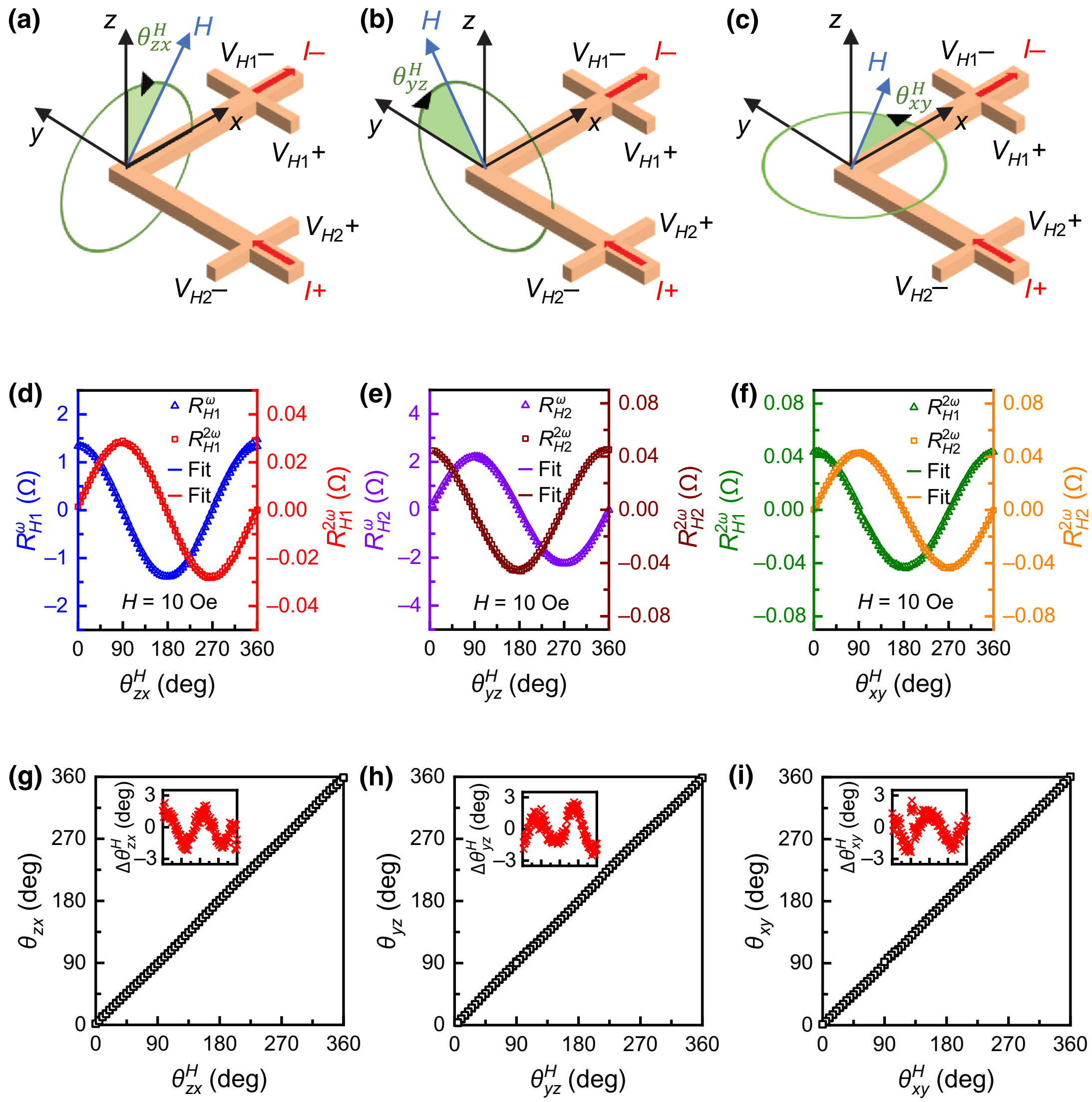

FIG. 5. (a)–(c) Measurement geometries with the field rotating in zx, yz, and xy planes, respectively. (d), (e) First- and second-harmonic Hall resistance of arm-X with the field rotating in the zx and yz planes, respectively. (f) Second-harmonic Hall resistance of arm-X and arm-Y with the field rotating in the xy plane. The field strength is fixed at 10 Oe. (g)–(i) Actual field angle (θ_{ij}^H) versus calculated field angle (θ_{ij}) in the full range of 360° when the field rotates in zx, yz, and xy planes, respectively ($i, j = x, y, z$). The insets show the angle errors.

as a function of θ_{xy}^H from 0° to 360° when the external field strength is 50 Oe. The corresponding relationships between the detected angle and actual field angle are shown in Figs. 6(c) and 6(d), respectively, with the angle error given in the insets. As can be seen, the maximum angle error increases to be 8° for θ_{zx}^H with an external field strength of 30 Oe. As can be seen from Fig. 6(a), the measured R_{H1}^{ω} and $R_{H1}^{2\omega}$ curves deviate from the cosine and sine fitting curves, which results in a larger angle error. However, the angle error for θ_{xy}^H remains less than 3° with an external field strength of 50 Oe, as shown in Figs. 6(b) and 6(d). The main reason for the larger angle error, especially for θ_{zx}^H (and θ_{yz}^H), is the crosstalk between vertical and longitudinal field components induced by the non-negligible higher-order effect at large fields (see the Appendix for details). The error can be reduced by removing the higher-order effect, as shown in Fig. 7.

Figure 7(a) shows the R_{H1}^{ω} and $R_{H1}^{2\omega}$ as a function of θ_{zx}^H from 0° to 360° when the external field strength is 30 Oe and fitting results using $R_H^{\omega} = R_0 + k_1 \cos\theta_{zx}^H + k_2 \cos 3\theta_{zx}^H$ and $R_H^{2\omega} = k_3 \sin\theta_{zx}^H + k_4 \sin 3\theta_{zx}^H$. Here,

$$k_1 = \frac{R_{\mathrm{AHE}}}{H_0}H - \frac{R_{\mathrm{AHE}}}{4H_0^3}H^3 - \frac{3I_0^2 R_{\mathrm{AHE}} A^2}{16H_0^3}H^3,$$

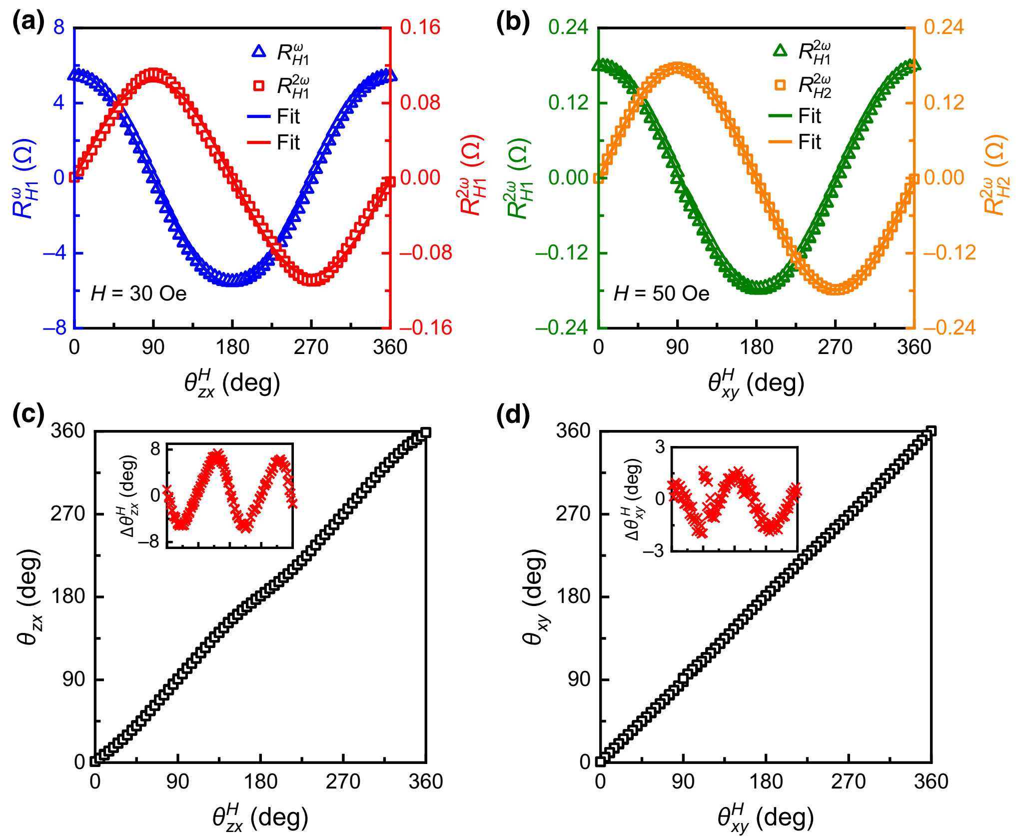

FIG. 6. (a) First- and second-harmonic Hall resistance of arm-X with a rotating field of 30 Oe in the zx plane. (b) Second-harmonic Hall resistance of arm-X and arm-Y with a rotating field of 50 Oe in the xy plane. The plots of actual field angle (θ^{H}_{ij}) versus calculated field angle (θ_{ij}) in the full range of 360° ($i, j = x, y, z$) corresponding to (a) and (b) are shown in (c) and (d), respectively. The insets are the angle errors.

$$k_2 = \frac{3I_0^2 R_{\mathrm{AHE}} A^2}{16H_0^3} H^3 - \frac{R_{\mathrm{AHE}}}{12H_0^3} H^3,$$

$$k_3 = -\frac{I_0 R_{\mathrm{AHE}} A}{2H_0} H + \frac{I_0^3 R_{\mathrm{AHE}} A^3}{8H_0^3} H^3 + \frac{I_0 R_{\mathrm{AHE}} A}{8H_0^3} H^3$$

and

$$k_4 = \frac{I_0 R_{AHE} A}{8H_0^3} H^3 - \frac{I_0^3 R_{\mathrm{AHE}} A^3}{24H_0^3} H^3$$

(see the Appendix for details). As can be seen, R^{ω}_{H1} and $R^{2\omega}_{H1}$ can be well fitted with $R_0 = 0.038\ \Omega$, $k_1 = 5.632\ \Omega$,

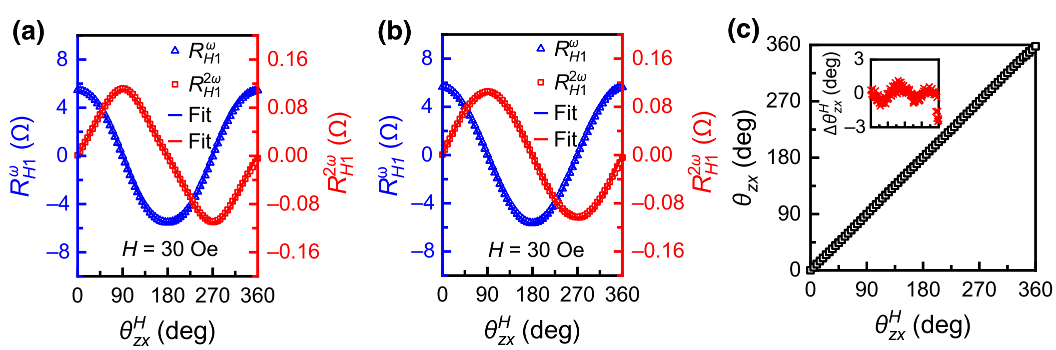

FIG. 7. (a) First- and second-harmonic Hall resistance of arm-X with the 30 Oe field rotating in the zx plane. First- and second-harmonic Hall resistance are fitted with Eq. (A4) (blue solid line) and Eq. (A5) (red solid line), respectively. (b) First- and second-harmonic Hall resistance without $k_2 \cos\ 3\theta^{\mathrm{H}}_{zx}$ and $k_4 \sin\ 3\theta^{\mathrm{H}}_{zx}$ components, respectively. (c) Actual field angle (θ^{H}_{zx}) versus calculated field angle (θ_{zx}) in the full range of 360° when the field rotates in the zx plane. The inset shows the angle error.

$k_2 = -0.154\ \Omega$, $k_3 = 0.104\ \Omega$, and $k_4 = -0.006\ \Omega$. The crosstalk between vertical and longitudinal field components induces $k_2 \cos 3\theta_{zx}^H$ in R_H^ω and $k_4 \sin 3\theta_{zx}^H$ in $R_H^{2\omega}$. Next, we subtracted $k_2 \cos 3\theta_{zx}^H$ and $k_4 \sin 3\theta_{zx}^H$ from R_{H1}^ω and $R_{H1}^{2\omega}$, respectively. As shown in Fig. 7(b), after the subtractions, R_{H1}^ω and $R_{H1}^{2\omega}$ can be well fitted with cosine and sine functions, respectively. Figure 7(c) shows the detected angle θ_{zx} which is calculated with $R_{H1}^\omega - k_2 \cos 3\theta_{zx}^H$ and $R_{H1}^{2\omega} - k_4 \sin 3\theta_{zx}^H$. As can be seen, the maximum angle error is less than 1° except for the few points near $\theta_{zx}^H = 360°$, which is presumably caused by the accuracy of sample rotator.

D. Vector mapping of a magnetic field generated by a permanent magnet

The results indicate that the L-shaped device can function as both a single-axial and biaxial sensor. To further demonstrate its capability as a vector magnetometer, we used the same device to map the field generated by a permanent magnet. Figure 8(a) shows the experimental setup where a cylindrical N35 permanent magnet ($B_s = 1.27$ T) with a diameter of 10 mm and thickness of 5 mm is attached to a nonmagnetic fixture with its N-pole pointing down. The L-shaped Hall device was placed on an xy-stage right below the magnet 33 mm from the bottom surface of the magnet and its center was aligned with that of the magnet. The arm-X and arm-Y of the device are aligned parallel with the two rails of the xy stage, and are indicated as the x- and y-axis, respectively, in Fig. 8(a). As shown in Fig. 8(b), by scanning the sensor over an area of 50 mm × 12 mm, we successfully obtain the vector field distribution on a plane that is located 33 mm below the magnet. The vectors are directly plotted from the field components, H_x, H_y, H_z, which were measured simultaneously using the Hall device through the harmonic Hall resistance $R_{H1}^{2\omega}$, $R_{H2}^{2\omega}$, and R_{H1}^{ω}. To check the accuracy of the mapping results, we calculated the amplitude (H) and polar (θ_H) and azimuthal (φ_H) angle of the field extracted from the measured field components, i.e., $H = (H_x^2 + H_y^2 + H_z^2)^{1/2}$, $\theta_H = \cos^{-1}(H_z/H)$, and $\varphi_H = \mathrm{atan2}(-H_x/(H_x^2 + H_y^2)^{1/2}, -H_y/(H_x^2 + H_y^2)^{1/2}) + \pi$, and compared them with the simulation results. Figures 8(c)–8(e) show the experimental data and the corresponding results simulated by the COMSOL MULTIPHYSICS software are shown in Figs. 8(f)–8(h), respectively. As can be seen, the measured field magnitude and angle are in good agreement with the simulation results. The results shown in Figs. 5 and 8 demonstrate clearly that the Hall device functions a vector magnetometer. Although we use 1.4 nm $Co_{20}Fe_{60}B_{20}$ as the sensing layer, a thinner layer can also be used if one wants to boost the liner range at a price of reduced sensitivity. It is worth pointing out that, owing to the use of multiple sensors in commercial Hall vector magnetometers, the spatial distance between any two sensors is typically larger than 150 μm [54–57]. In contrast, in the device presented in this work, the distance between the two Hall cross is 70 $\mu\mu$m and it can be further reduced to less than 30 μm (not shown here). The significant enhancement of spatial resolution will help to extend the application fields of vector magnetometer.

Before we conclude, we mention that several SOT-based magnetic sensors have been reported previously from both ours and other groups [42,58–61]. In Table I, we compare the detection mode, detection principle, and field range of these sensors. The first type of sensor is a linear sensor which can only detect field along a single axis (mode 1 in Table I). We have previously reported two types of SOT-enabled linear sensors, namely the spin Hall magnetoresistance (SMR) sensor for weak field detection [58,59], and the spin-torque gate (STG) sensor for intermediate-range field detection [42]. Both types of sensors exhibit a field angle dependence similar to that of a giant magnetoresistance sensor, and therefore they can be used for angle sensing as well (mode 2 in Table I). In addition, we have also developed a SOT-based angular position sensor using two Hall crosses operating under pulsed current [60]. The sensor can detect the direction of a rotational field on the xy plane, with a field strength from 500 to 2000 Oe. Recently, Li et al. reported a SOT-based Hall device which can measure IP and OP fields separately (Mode 3 in Table I) in a relatively small field range [61]. The IP field detection is based on current-induced domain wall motion, and Joule heating is used to suppress the hysteresis in the z-direction. It is important to note that separate measurement of individual field components is different from simultaneous measurements of three components because the latter must deal with crosstalk among different field components. Crosstalk is unavoidable in SOT-based sensors because the SOT effective field is required for detecting the IP field components. The crosstalk causes the decrease of detectable field range for field along arbitrary directions in a three-dimensional space, which is absent when the field is only along a single coordinate axis (modes 1 and 3 in Table I). As discussed in the appendix, the output signal of SOT-based anomalous Hall sensor may be written as $V \approx aH_z + bH_x + cH_x^2H_z + dH_z^2H_x + eH_z^3 + fH_x^3$ (when current is in the x-direction) and $V \approx aH_z + bH_y + cH_y^2H_z + dH_z^2H_y + eH_z^3 + fH_y^3$ (when current is in the y-direction). Here, a, b, c, d, e, and f are field-independent constants. The third and fourth terms are crosstalk terms which only appear when multiple field components are present. This aspect is overlooked in previous work as the measurement of a specific field component was performed without the presence of other field components. In contrast, here we have demonstrated a device that can measure all the three field components simultaneously, meaning that it can function in all detection modes listed in Table I, ranging from single-axial to biaxial and triaxial sensing. In that sense, the harmonic Hall vector magnetometer represents a fully

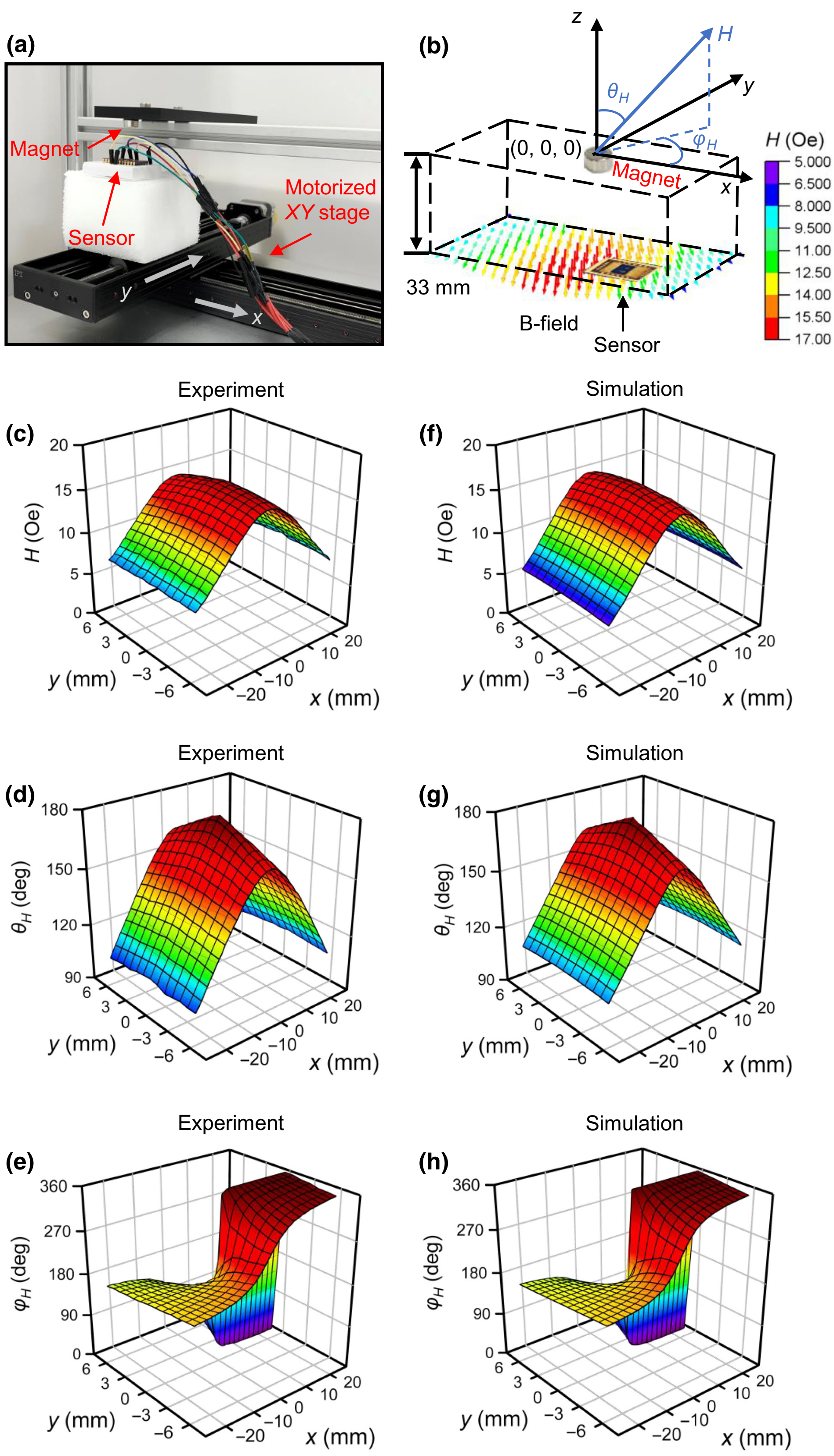

FIG. 8. (a) Experimental setup for vector mapping of the magnetic field generated by a permanent magnet. (b) Measurement configuration according to the setup in (a). Also shown is the measured vector field distribution over an area of 50 mm × 12 mm on the *xy* plane. (c)–(e) Measured amplitude, polar and azimuthal angle of the magnetic field, respectively. (f)–(h) Simulated amplitude, polar and azimuthal angle of the magnetic field, respectively.

TABLE I. Comparison of SOT-based magnetic field sensors.

Detection Mode	Detection range	Detection principle	Linear range	Remarks
Mode 1: Field along single axis	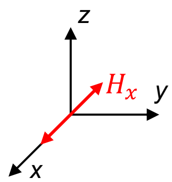	SOT biasing and SMR	±1 Oe	SMR sensor [58,59]
		SOT-driven switching	±10 Oe	STG sensor [42]
Mode 2: Field along a circle on xy plane (angle sensor)	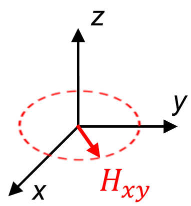	Angular position sensing has been demonstrated using SMR sensor [58,59], STG sensor [42], and SO—driven Hall sensor [60] under a field strength of 1 Oe, 20 Oe, and 500–2000 Oe, respectively.		
Mode 3: Field along 3 coordinate axes	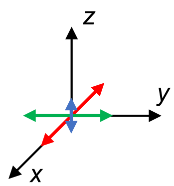	Pulsed current-induced DW motion and detection	H_x : ±10 Oe H_y : ±10 Oe H_z : ±4 Oe	Measure H_x, H_y, and H_z, separately [61]
Mode 4: Field on three coordinate planes	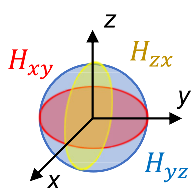	SOT effective field and harmonic AHE	H_x : ±100 Oe H_y : ±100 Oe H_z : ±50 Oe H_{zx} : 30 Oe H_{yz} : 30 Oe H_{xy} : 50 Oe	Pseudo-3D field mapping (this work)
Mode 5: Field in three-dimensional space	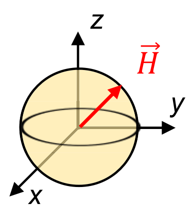	SOT effective field and harmonic AHE	20 Oe in all directions	Full 3D vector field mapping (this work)

functional vector magnetometer based on a single planar device.

IV. CONCLUSIONS

In summary, we have proposed and demonstrated a fully functional single-device vector magnetometer enabled by the SOT and harmonic technique. The harmonic Hall vector magnetometer is an L-shaped Hall device with two orthogonal arms. By measuring the first- and second-harmonic Hall resistance of both arms, we can determine the three components of a vector field simultaneously. In addition to angle sensing on each coordinate plane, we have also shown that the proposed device is able to sense a vector field in any direction in three-dimensional space. Its simple configuration and high accuracy show its great potential in various fields requiring vector field measurements such as navigation, Internet of things, smart electronics, and many other traditional and emerging applications.

ACKNOWLEDGMENTS

This project is supported by the Ministry of Education, Singapore, under its Tier 2 Grants (Grants No. MOE2018-T2-1-076 and No. MOE2017-T2-2-011) and an ARTIC Grant (HFM-RP4) from the National University of Singapore.

APPENDIX: CROSSTALK BETWEEN VERTICAL AND LONGITUDINAL FIELD COMPONENTS

The results in Fig. 6 show that the angle error increases significantly at large field, especially for the angle detection on *zx* or *yz* plane. This is caused by the crosstalk induced by the non-negligible higher-order terms at large field. When H_z or H_x is large, the term with $n = 2$ in Eq. (5) is non-negligible and it should be duly considered, i.e.,

$$V_H \approx I_0 R_0 \sin\omega t + I_0 R_{\mathrm{AHE}} \sin\omega t \times \left\{ \frac{1}{H_0}(H_z + AH_x I_0 \sin\omega t) - \frac{1}{3}\left[\frac{1}{H_0}(H_z + AH_x I_0 \sin\omega t)\right]^3 \right\}. \tag{A1}$$

By expanding Eq. (A1), we can obtain the first and second-harmonic Hall resistance as follows:

$$R_H^{\omega} = R_0 + \frac{R_{\mathrm{AHE}}}{H_0}H_z - \frac{1}{3}\frac{R_{\mathrm{AHE}}}{H_0^3}H_z^3 - \frac{3}{4}I_0^2 R_{\mathrm{AHE}}\frac{A^2}{H_0^3}H_z H_x^2, \tag{A2}$$

$$R_H^{2\omega} = -\frac{1}{2}I_0\frac{R_{\mathrm{AHE}}}{H_0}AH_x + \frac{1}{6}I_0^3\frac{R_{\mathrm{AHE}}}{H_0^3}A^3H_x^3 + \frac{1}{2}I_0\frac{R_{\mathrm{AHE}}}{H_0^3}AH_z^2H_x. \tag{A3}$$

In the case of a rotating field in the *xz* plane, H_x and H_z can be written as $H_x = H \sin\theta_{zx}^H$ and $H_z = H\cos\theta_{zx}^H$, respectively, where H is the field strength and θ_{zx}^H is the angle between the rotating field and *z*-axis on the *zx* plane. Using the trigonometric identity, R_H^{ω} and $R_H^{2\omega}$ can be further written as

$$R_H^{\omega} = R_0 + k_1\cos\theta_{zx}^H + k_2\cos 3\theta_{zx}^H, \tag{A4}$$

$$R_H^{2\omega} = k_3\sin\theta_{zx}^H + k_4\sin 3\theta_{zx}^H, \tag{A5}$$

where

$$k_1 = \frac{R_{\mathrm{AHE}}}{H_0}H - \frac{R_{\mathrm{AHE}}}{4H_0^3}H^3 - \frac{3I_0^2R_{\mathrm{AHE}}A^2}{16H_0^3}H^3,$$

$$k_2 = \frac{3I_0^2R_{\mathrm{AHE}}A^2}{16H_0^3}H^3 - \frac{R_{\mathrm{AHE}}}{12H_0^3}H^3,$$

$$k_3 = -\frac{I_0R_{\mathrm{AHE}}A}{2H_0}H + \frac{I_0^3R_{\mathrm{AHE}}A^3}{8H_0^3}H^3 + \frac{I_0R_{\mathrm{AHE}}A}{8H_0^3}H^3$$

and

$$k_4 = \frac{I_0R_{\mathrm{AHE}}A}{8H_0^3}H^3 - \frac{I_0^3R_{\mathrm{AHE}}A^3}{24H_0^3}H^3,$$

where A is defined in the main text. As can be seen from Eqs. (A4) and (A5), $k_2\cos 3\theta_{zx}^H$ and $k_4 \sin 3\theta_{zx}^H$ induced by the higher-order effect become non-negligible with a large magnetic field strength, resulting in the deviation of R_H^{ω} and $R_H^{2\omega}$ curve from the cosine and sine shape, respectively.

[1] J. Heremans, Solid state magnetic field sensors and applications, J. Phys. D: Appl. Phys. **26**, 1149 (1993).

[2] P. Ripka and M. Janosek, Advances in Magnetic Field Sensors, IEEE Sens. J. **10**, 1108 (2010).

[3] J. Lenz and S. Edelstein, Magnetic sensors and their applications, IEEE Sens. J. **6**, 631 (2006).

[4] S. Parkin, J. Xin, C. Kaiser, A. Panchula, K. Roche, and M. Samant, Magnetically engineered spintronic sensors and memory, Proc. IEEE **91**, 661 (2003).

[5] C. Zheng, K. Zhu, S. C. de Freitas, J. Y. Chang, J. E. Davies, P. Eames, P. P. Freitas, O. Kazakova, C. Kim, C. W. Leung, *et al.*, Magnetoresistive sensor development roadmap (non-recording applications), IEEE Trans. Magn. **55**, 1 (2019).

[6] A. V. Silva, D. C. Leitao, J. Valadeiro, J. Amaral, P. P. Freitas, and S. Cardoso, Linearization strategies for high sensitivity magnetoresistive sensors, Eur. Phys. J.: Appl. Phys. **72**, 10601 (2015).

[7] G. Xiao, in *Spintronics Handbook: Spin Transport and Magnetism*, 2nd ed., edited by I. Ž. Evgeny and Y. Tsymbal (CRC Press, Boca Raton, 2019), pp. 385.

[8] S. Macintyre, A portable low noise low frequency three-axis search coil magnetometer, IEEE Trans. Magn. **16**, 761 (1980).

[9] B. J. Anderson, M. H. Acuña, D. A. Lohr, J. Scheifele, A. Raval, H. Korth, and J. A. Slavin, in *Space Sci. Rev.*, edited by D. L. Domingue, Russell C. T. (Springer, New York, NY, 2007), pp. 417.

[10] M. H. Acuna, The Magsat precision vector magnetometer, Johns Hopkins APL Tech. Dig. **1**, 210 (1980).

[11] C. Wouters, V. Vranković, C. Rössler, S. Sidorov, K. Ensslin, W. Wegscheider, and C. Hierold, Design and fabrication of an innovative three-axis Hall sensor, Sens. Actuators, A **237**, 62 (2016).

[12] C. Schott, R. Racz, A. Manco, and N. Simonne, CMOS single-chip electronic compass with microcontroller, IEEE J. Solid-State Circuits **42**, 2923 (2007).

[13] C. Becker, D. Karnaushenko, T. Kang, D. Karnaushenko Dmitriy, M. Faghih, A. Mirhajivarzaneh, and G. Schmidt Oliver, Self-assembly of highly sensitive 3D magnetic field vector angular encoders, Sci. Adv. **5**, eaay7459 (2019).

[14] X. T. Trinh, J.-T. Jeng, C.-C. Lu, M.-J. Lan, B.-C. Chen, J. H. Hsu, V. S. Luong, and H.-Y. Hsu, Miniature tri-axis magnetometer with in-plane GMR sensors, IEEE Trans. Magn. **53**, 1 (2017).

[15] J. T. Jeng, C. Y. Chiang, C. H. Chang, and C. C. Lu, Vector magnetometer with dual-bridge GMR sensors, IEEE Trans. Magn. **50**, 1 (2014).

[16] X. Li, X. Zhao, and D. Wen, Characteristics of a magnetic field sensor with a concentrating-conducting magnetic flux structure, Sensors **19**, 4498 (2019).

[17] S. Hong, M. S. Grinolds, L. M. Pham, D. Le Sage, L. Luan, R. L. Walsworth, and A. Yacoby, Nanoscale magnetometry with NV centers in diamond, MRS Bull. **38**, 155 (2013).

[18] L. Rondin, J. P. Tetienne, T. Hingant, J. F. Roch, P. Maletinsky, and V. Jacques, Magnetometry with nitrogen-vacancy defects in diamond, Rep. Prog. Phys. **77**, 056503 (2014).

[19] J. M. Schloss, J. F. Barry, M. J. Turner, and R. L. Walsworth, Simultaneous broadband vector magnetometry using solid-state spins, Phys. Rev. Appl. **10**, 034044 (2018).

[20] A. Manchon, J. Železný, I. M. Miron, T. Jungwirth, J. Sinova, A. Thiaville, K. Garello, and P. Gambardella, Current-induced spin-orbit torques in ferromagnetic and antiferromagnetic systems, Rev. Mod. Phys. **91**, 035004 (2019).

[21] R. Ramaswamy, J. M. Lee, K. Cai, and H. Yang, Recent advances in spin-orbit torques: Moving towards device applications, Appl. Phys. Rev. **5**, 031107 (2018).

[22] A. Hirohata, K. Yamada, Y. Nakatani, I.-L. Prejbeanu, B. Diény, P. Pirro, and B. Hillebrands, Review on spintronics: Principles and device applications, J. Magn. Magn. Mater. **509**, 166711 (2020).

[23] C. Song, R. Zhang, L. Liao, Y. Zhou, X. Zhou, R. Chen, Y. You, X. Chen, and F. Pan, Spin-orbit torques: Materials, mechanisms, performances, and potential applications, Prog. Mater. Sci. **118**, 100761 (2021).

[24] Q. Shao, P. Li, L. Liu, H. Yang, S. Fukami, A. Razavi, H. Wu, K. Wang, F. Freimuth, Y. Mokrousov, *et al.*, Roadmap of spin–orbit torques, IEEE Trans. Magn. **57**, 1 (2021).

[25] T. Neuberger, B. Schöpf, H. Hofmann, M. Hofmann, and B. von Rechenberg, Superparamagnetic nanoparticles for biomedical applications: Possibilities and limitations of a new drug delivery system, J. Magn. Magn. Mater. **293**, 483 (2005).

[26] Y. Jang, C. Nam, J. Y. Kim, B. K. Cho, Y. J. Cho, and T. W. Kim, Magnetic field sensing scheme using CoFeBâĹŢMgOâĹŢCoFeB tunneling junction with superparamagnetic CoFeB layer, Appl. Phys. Lett. **89**, 163119 (2006).

[27] J. F. Feng, J. Y. Chen, M. Venkatesan, G. Feng, X. F. Han, and J. M. D. Coey, Superparamagnetism in MgO-based magnetic tunnel junctions with a thin pinned ferromagnetic electrode, Phys. Rev. B **81**, 205212 (2010).

[28] N. Miyakawa, D. C. Worledge, and K. Kita, Impact of Ta diffusion on the perpendicular magnetic anisotropy of Ta/CoFeB/MgO, IEEE Magn. Lett. **4**, 1000104 (2013).

[29] C. C. Tsai, C. W. Cheng, M. C. Tsai, and G. Chern, Superparamagnetic states and perpendicular magnetic anisotropy in ultrathin MgO/CoFeB/Ta structures, IEEE Trans. Magn. **50**, 1 (2014).

[30] L. Malkinski (ed.), *Advanced magnetic materials* (IntechOpen, London, 2012).

[31] J. Takács, A phenomenological mathematical model of hysteresis, COMPEL Int. J. Comput. Math. Electr. Electron. Eng. **20**, 1002 (2001).

[32] K. Y. Camsari, S. Salahuddin, and S. Datta, Implementing p-bits with embedded MTJ, IEEE Electron Device Lett. **38**, 1767 (2017).

[33] K. Y. Camsari, R. Faria, B. M. Sutton, and S. Datta, Stochastic *p*-bits for invertible logic, Phys. Rev. X **7**, 031014 (2017).

[34] W. A. Borders, A. Z. Pervaiz, S. Fukami, K. Y. Camsari, H. Ohno, and S. Datta, Integer factorization using stochastic magnetic tunnel junctions, Nature **573**, 390 (2019).

[35] M. Bapna, B. Parks, S. D. Oberdick, H. Almasi, W. Wang, and S. A. Majetich, Spin-orbit-torque switching in 20-nm perpendicular magnetic tunnel junctions, Phys. Rev. Appl. **10**, 024013 (2018).

[36] P. Debashis, R. Faria, K. Y. Camsari, S. Datta, and Z. Chen, Correlated fluctuations in spin orbit torque coupled perpendicular nanomagnets, Phys. Rev. B **101**, 094405 (2020).

[37] L. Liu, C.-F. Pai, Y. Li, H. W. Tseng, D. C. Ralph, and R. A. Buhrman, Spin-torque switching with the giant spin Hall effect of tantalum, Science **336**, 555 (2012).

[38] K.-S. Lee, S.-W. Lee, B.-C. Min, and K.-J. Lee, Threshold current for switching of a perpendicular magnetic layer induced by spin Hall effect, Appl. Phys. Lett. **102**, 112410 (2013).

[39] S. Pizzini, J. Vogel, S. Rohart, L. D. Buda-Prejbeanu, E. Jué, O. Boulle, I. M. Miron, C. K. Safeer, S. Auffret, G. Gaudin, *et al.*, Chirality-induced asymmetric magnetic nucleation in Pt/Co/AlOx ultrathin microstructures, Phys. Rev. Lett. **113**, 047203 (2014).

[40] O. J. Lee, L. Q. Liu, C. F. Pai, Y. Li, H. W. Tseng, P. G. Gowtham, J. P. Park, D. C. Ralph, and R. A. Buhrman, Central role of domain wall depinning for perpendicular magnetization switching driven by spin torque from the spin Hall effect, Phys. Rev. B **89**, 024418 (2014).

[41] M. Mogi, K. Yasuda, R. Fujimura, R. Yoshimi, N. Ogawa, A. Tsukazaki, M. Kawamura, K. S. Takahashi, M. Kawasaki, and Y. Tokura, Current-induced switching of proximity-induced ferromagnetic surface states in a topological insulator, Nat. Commun. **12**, 1404 (2021).

[42] H. Xie, X. Chen, Z. Luo, and Y. Wu, Spin torque gate magnetic field sensor, Phys. Rev. Appl. **15**, 024041 (2021).

[43] J. Sinha, M. Gruber, M. Kodzuka, T. Ohkubo, S. Mitani, K. Hono, and M. Hayashi, Influence of boron diffusion on the perpendicular magnetic anisotropy in Ta|CoFeB|MgO ultrathin films, J. Appl. Phys. **117**, 043913 (2015).

[44] X.-J. Li, S.-L. Jiang, J.-Y. Zhang, Q.-Q. Liu, Y.-W. Liu, J.-C. Zhao, Z.-L. Wu, C. Feng, M.-H. Li, and G.-H. Yu, Enhanced post-annealing stability of perpendicular Ta/CoFeB/Mg/MgO multilayers by inhibiting Ta diffusion, Appl. Surf. Sci. **365**, 275 (2016).

[45] Y. Aleksandrov, C. Fowley, E. Kowalska, V. Sluka, O. Yıldırım, J. Lindner, B. Ocker, J. Fassbender, and A. M. Deac, Evolution of the interfacial magnetic anisotropy in MgO/CoFeB/Ta/Ru based multilayers as a function of annealing temperature, AIP Adv. **6**, 065321 (2016).

[46] Y. Yang, H. Xie, Y. Xu, Z. Luo, and Y. Wu, Multistate magnetization switching driven by spin current from a ferromagnetic layer, Phys. Rev. Appl. **13**, 034072 (2020).

[47] S. B. Wu, T. Zhu, X. F. Yang, and S. Chen, The anomalous Hall effect in the perpendicular Ta/CoFeB/MgO thin films, J. Appl. Phys. **113**, 17C717 (2013).

[48] T. Zhu, P. Chen, Q. H. Zhang, R. C. Yu, and B. G. Liu, Giant linear anomalous Hall effect in the perpendicular CoFeB thin films, Appl. Phys. Lett. **104**, 202404 (2014).
[49] S. Zhang, Y. Su, X. Li, R. Li, W. Tian, J. Hong, and L. You, Spin-orbit-torque-driven multilevel switching in Ta/CoFeB/MgO structures without initialization, Appl. Phys. Lett. **114**, 042401 (2019).
[50] M. Endo, S. Kanai, S. Ikeda, F. Matsukura, and H. Ohno, Electric-field effects on thickness dependent magnetic anisotropy of sputtered MgO/Co40Fe40B20/Ta structures, Appl. Phys. Lett. **96**, 212503 (2010).
[51] V. B. Naik, H. Meng, and R. Sbiaa, Thick CoFeB with perpendicular magnetic anisotropy in CoFeB-MgO based magnetic tunnel junction, AIP Adv. **2**, 042182 (2012).
[52] J. Kim, J. Sinha, M. Hayashi, M. Yamanouchi, S. Fukami, T. Suzuki, S. Mitani, and H. Ohno, Layer thickness dependence of the current-induced effective field vector in Ta|CoFeB|MgO, Nat. Mater. **12**, 240 (2013).
[53] P. G. Gowtham, G. M. Stiehl, D. C. Ralph, and R. A. Buhrman, Thickness-dependent magnetoelasticity and its effects on perpendicular magnetic anisotropy in Ta/CoFeB/MgO thin films, Phys. Rev. B **93**, 024404 (2016).
[54] https://www.lakeshore.com/products/categories/specification/magnetic-products/hall-(magnetic)-sensors/2dex-hall-sensors
[55] https://www.infineon.com/cms/en/product/sensor/magnetic-sensors/magnetic-position-sensors/3d-magnetics/tlv493d-a2bw/
[56] https://www.metrolab.com/products/thm1176-three-axis-hall-magnetometer/
[57] https://www.metrolab.com/products/tfm1186-three-axis-fluxgate-magnetometer/
[58] Y. Xu, Y. Yang, M. Zhang, Z. Luo, and Y. Wu, Ultrathin all-in-one spin Hall magnetic sensor with built-in AC excitation enabled by spin current, Adv. Mater. Technol. **3**, 1800073 (2018).
[59] Y. Xu, Y. Yang, H. Xie, and Y. Wu, Spin Hall magnetoresistance sensor using Au_xPt_{1-x} as the spin-orbit torque biasing layer, Appl. Phys. Lett. **115**, 182406 (2019).
[60] Z. Luo, Y. Xu, Y. Yang, and Y. Wu, Magnetic angular position sensor enabled by spin-orbit torque, Appl. Phys. Lett. **112**, 262405 (2018).
[61] R. Li, S. Zhang, S. Luo, Z. Guo, Y. Xu, J. Ouyang, M. Song, Q. Zou, L. Xi, X. Yang, *et al.*, A spin–orbit torque device for sensing three-dimensional magnetic fields, Nat. Electron. **4**, 179 (2021).